The time-resolved natural flow field of a fluidic oscillator — **Source link** ↗

Rene Woszidlo, Florian Ostermann, Christian Navid Nayeri, Christian Oliver Paschereit

Institutions: University of Kansas, Technical University of Berlin

Related papers:

- Experimental study of the internal flow structures inside a fluidic oscillator

- Phase-Averaging Methods for the Natural Flowfield of a Fluidic Oscillator

- Discrete Sweeping Jets as Tools for Improving the Performance of the V-22

- Lagrangian coherent structures in the flow field of a fluidic oscillator

- Cavity Resonance Suppression Using Miniature Fluidic Oscillators

Woszidlo, R.; Ostermann, F.; Nayeri, C. N.; Paschereit, C. O.

The time-resolved natural flow field of a fluidic oscillator

WISSEN IM ZENTRUM
UNIVERSITÄTSBIBLIOTHEK

Technische
Universität
Berlin

The Time-Resolved Natural Flow Field of a Fluidic Oscillator

R. Woszidlo · F. Ostermann · C.N. Nayeri · C.O. Paschereit

Abstract The internal and external flow field of a fluidic oscillator with two feedback channels are examined experimentally within the incompressible flow regime. A scaled-up device with a square outlet nozzle is supplied with pressurized air and emits a spatially oscillating jet into quiescent environment. Time-resolved information are obtained by phase-averaging pressure and PIV data based on an internal reference signal. The temporal resolution is better than a phase angle of 3°. A detailed analysis of the internal dynamics reveals that the oscillation mechanism is based on fluid feeding into a separation bubble between the jet and mixing chamber wall which pushes the jet to the opposite side. The total volume of fluid transported through one feedback channel during one oscillation cycle matches the total growth of the separation bubble from its initial size to its maximum extent. Although the oscillation frequency increases linearly with supply rate, sudden changes in the internal dynamics are observed. These changes are caused by a growth in reversed flow through the feedback channels. The time-resolved properties of the emitted jet such as instantaneous jet width and exit velocity are found to oscillate substantially during one oscillation cycle. Furthermore, the results infer that the jet's oscillation pattern is approximately sinusoidal with comparable residence and switching times.

Rene Woszidlo
The University of Kansas, Aerospace Department
1530 W 15th St
Lawrence, KS 66045, USA
E-mail: rene@ku.edu

Florian Ostermann
Technische Universität Berlin
Müller-Breslau-Straße 8
10623 Berlin, Germany
E-mail: florian.ostermann@tu-berlin.de

1 Introduction

Fluidic oscillators are devices which emit a continuous but spatially oscillating jet when supplied with a pressurized fluid. These oscillations are self-induced and self-sustained, solely based on the internal fluid dynamics without requiring any moving parts. A snapshot of an oscillating water jet is illustrated in figure 1 (right) which is emitted by an oscillator similar in design to the geometry discussed in this study. Figure 1 (left) conceptually illustrates the internal dynamics. The main jet enters into a mixing chamber where it attaches to either side wall due to the Coanda effect. A portion of the main jet stream returns through the respective feedback channel to the oscillator's inlet where it causes the jet to detach and flip to the opposite side. There, the same process occurs to complete one oscillation cycle. The exact details of the oscillation mechanism are addressed in the current study. The oscillation frequency may range from the order of 1 Hz up to several kHz (Gregory et al 2007) depending on the oscillator's size, geometry, supply rate, and the fluid's properties.

Fluidic oscillators were developed more than half a century ago at the Harry Diamond Research Laboratories with the initial intention of providing the basis for control circuits as fluid logic elements. With the rapid development of electronic alternatives, fluidic devices became obsolete and have mainly been used for water applications such as windshield washer nozzles, sprinklers, and shower heads. Since their initial development, various types and designs of fluidic oscillators have been patented (e.g. Stouffer 1979, Luxton and Nathan 1991,
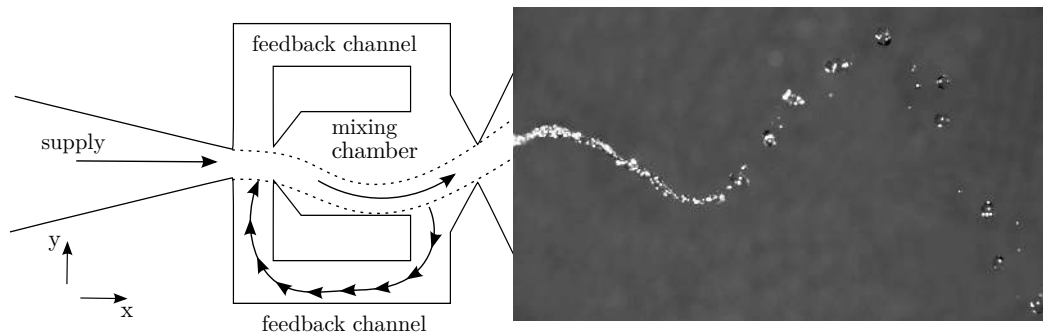
and Raghu 2001). The main difference between various designs is the number of feedback channels which also determines the underlying mechanism that causes the jet to oscillate. For the design without feedback channels (Gregory et al 2007; Raghu 2001), the jet's oscillations are solely based on the shear layer instability between two interacting jets. The second category of fluidic oscillators incorporates just one feedback loop (e.g. Spyropoulos 1964). The oscillation mechanism for this category is based on a pressure signal being sent through one feedback channel which draws the jet over to the opposite side. Therefore, the oscillatory behavior is mainly governed by the geometry of the feedback channel. The current study focuses on an oscillator with two feedback loops where a flow of fluid through the feedback channels causes the oscillations of the main jet (figure 1).

An extensive review of the historical development and contemporary research of fluidic oscillators was presented by Gregory and Tomac (2013). In recent years, these devices have gained renewed interest as flow control actuators. Numerous studies have demonstrated their potential for separation control (e.g. Seele et al 2009, Cerretelli and Kirtley 2009, Phillips and Wygnanski 2013, and Woszidlo et al 2014), combustion control (e.g. Guyot et al 2009), and noise control (e.g. Raman and Raghu 2004). Although fluidic oscillators have been successfully employed for flow control, the information available on their fundamental internal and external dynamics remain limited. Experimental studies are challenging due to their commonly small size which is associated with high frequencies and high exit velocities. Furthermore, no external trigger is available to phase-average the data. The oscillations are accompanied by natural fluctuations which add to the difficulties of obtaining time-resolved information on the flow field. Some initial insight was provided by a few recent studies. Gregory et al (2009) employed a secondary system (i.e. a piezoelectric bender) to control the jet oscillations which provided them with an external trigger signal. However, with this system the oscillations were not controlled by

the natural internal dynamics. A design similar to the one utilized in the current study was investigated by Bobusch et al (2013a) with water as a working fluid. Using water lowers the oscillation frequency and exit velocity for a given Reynolds number and circumvents compressibility effects. The method of proper orthogonal decomposition was employed to obtain time-resolved information on the internal flow field only. Despite limited temporal and spatial resolution, Bobusch et al (2013a) provided insight into the internal dynamics for the first time. A novel approach to obtaining time-resolved data on a fluidic oscillator with one feedback channel was documented by Wassermann et al (2013) who employed phase-locked three-dimensional three-components magnetic resonance velocimetry. They also noted the challenges of triggering into the natural oscillations of the device. The precursor of the current study was presented by Gaertlein et al (2014) with a preliminary analysis of the time-resolved internal and external flow field of a fluidic oscillator. Numerical studies have been sparse because they are burdened by the absence of a suitable data set for proper validation. A numerical parametric study by Bobusch et al (2013b) addressed the effects of some geometric features. Beside understanding the internal dynamics of fluidic oscillators, the external properties of oscillating jets are of crucial interest for the wide range of possible applications. The main question on how an oscillating jet interacts with a freestream has yet to be answered.

The presented work aims to improve the detailed understanding of fluidic oscillators by experimentally examining the incompressible time-resolved internal and external flow field. The natural flow field is phase-averaged based on the reference signal method developed by Ostermann et al (2015a). The following sections describe the experimental setup and data analysis methods. The time-resolved flow field is discussed in section 4 by evaluating the detailed dynamics and underlying mechanisms. In view of potential applications, emphasis is placed on the oscillation pattern of the external jet.
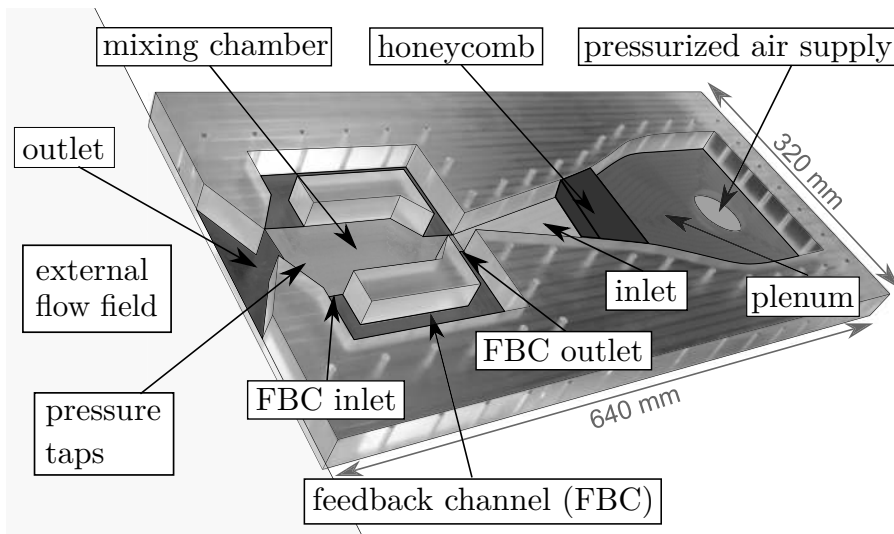
Fig. 2 Examined fluidic oscillator with denotations of main regions.

2 Setup and Instrumentation

The particular fluidic oscillator examined in this study is illustrated in figure 2 (left). The oscillator is scaled up in comparison to previous flow control applications (e.g., Woszidlo and Wygnanski 2011) in order to reduce the oscillation frequency and exit velocity, and to improve the visual accessibility. Optical access is enabled by machining the oscillator out of acrylic glass with a constant cavity depth of 25 mm. A cover plate (also made from acrylic glass) ensures an airtight seal. Compressed air is supplied into the plenum and monitored by a digital mass flow meter (F-203AV by Bronkhorst®-Mättig) with an accuracy better than 0.6 % full scale. The average temperature of the supplied air is 293 K. A temperature sensor is installed inside the pressure supply system to allow a continuous monitoring and to ensure the correct calibration conditions of the mass flow meter. The plenum's width contracts to the smallest inlet diameter with a ratio of 10 to 1. A piece of honeycomb upstream of the inlet ensures homogenous inflow conditions. The internal sections of the oscillator are marked in figure 2 (left) to be referenced throughout this paper. The square outlet of the oscillator is 25 mm × 25 mm which equates to a hydraulic diameter of $d_h = 25$ mm.

Inside the fluidic oscillator, 55 small orifices are distributed symmetrically to measure the time-resolved pressure. The pressure transducers (HDO Series by Sensortechnics) have a range of ±2000 Pa with a response time of 0.1 ms and an accuracy better than 0.2 % full scale. The sampling rate is fixed at 16 kHz which is three orders of magnitude higher than the oscillation frequency. The orifice diameter (0.8 mm) and length of the connection to the transducer (20 mm) are optimized to avoid
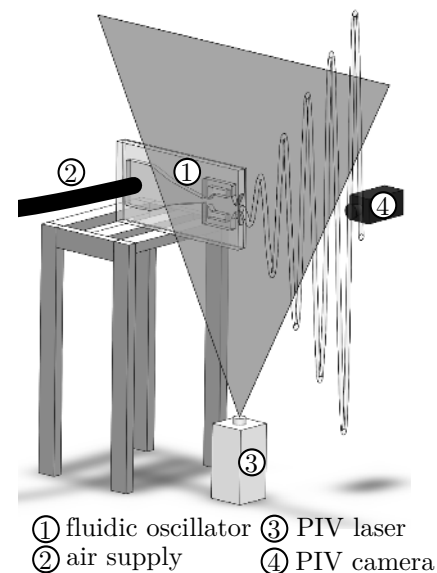

① fluidic oscillator ③ PIV laser
② air supply ④ PIV camera

Fig. 3 Schematic of the general setup

resonance effects and amplitude reduction by employing the calculation of the dynamic response of tubes. Even for the highest oscillation frequency (≈ 23 Hz), the expected phase delay is negligible. All pressure measurements are recorded simultaneously with a multichannel DAQ system from National Instruments™.

The fluidic oscillator is positioned on a pedestal so that the jet emits into unobstructed, quiescent environment (figure 3). The internal and external flow field are measured with Particle Image Velocimetry (PIV) by means of one high-speed camera (Photron Fastcam SA1.1) with a resolution of one megapixel and a 60 mJ Nd:YLF Laser (Quantronix Darwin Duo 100). The laser sheet penetrates the oscillator and the external flow field through the plane of symmetry. An aerosol generator

is integrated into the air supply system to seed the jet with particles less than 1 µm in size. Prior to measurements of the external flow field, the system is run for a sufficiently long time to distribute enough seeding throughout the laboratory so that the entrained air also contains seeding particles. The PIV sampling rate is constant at 1.5 kHz to record a total of 10,920 double pictures per test case. This amount of pictures enables a high temporal resolution during the phase-averaging process. Despite the constant PIV sampling rate, no phase-locking occurs due to the natural fluctuations in oscillation frequency. The post-processing of the PIV data is performed by using the commercial software PIVview2C 3.5. The interrogation window size is set to 16×16 pixels with an overlap of 50 % for the external flow field and 12×12 pixels with an overlap of 50 % for the internal flow field. This yields a spatial resolution of approximately 2 mm.

As expected from the different refractive indices of air and acrylic glass, the illumination of the internal cavities is non-homogeneous. In order to maximize data quality, measurements with different laser positions yield results for different areas of the internal geometry. These sections are individually phase-averaged through the process described in the following section and then phase-aligned based on the simultaneously recorded pressure data. The overlap regions are evaluated to assess the quality of the individual measurements which deviate less than 5 % and then averaged to provide a smooth transition. Through this process the entire internal flow field is spatially resolved. A similar process is applied to the external flow field to improve the spatial resolution. Four measurement windows (two in x-direction and two in y-direction) are recorded with a 10 % overlap in y-direction and a 20 % overlap in x-direction. The combination of these four windows yields the external flow field over 20 nozzle diameters.

3 Data Analysis

In order to obtain time-resolved flow field information with a high quality, the measurement data are phase-averaged. Ostermann et al (2015a) evaluated various phase-averaging methods for the specific application on a fluidic oscillator. They employed the same experimental setup and measurement techniques as in the present study. Two methods were identified to yield the most accurate results. The first method is based on proper orthogonal decomposition which does not require any time-resolved data. However, the entire jet oscillation has to be covered within one PIV window which limits the spatial resolution. Therefore, the second method is applied which is based on using pressure

data as a reference signal to identify the phase angle of each individual PIV snapshot in each measurement window. The most suitable reference signal is found to be the differential signal between two pressure sensors positioned symmetrically in the feedback channel inlets (figure 4, left). Because the feedback tube acts similar to a resonator with open ends, a high resonance frequency (one order of magnitude higher than the oscillation frequency) is imposed on the pressure signal. A numerical low pass filter is applied forward and backward to reduce the noise while maintaining phase and amplitude information. The entire reference signal is correlated with a segment of the same signal. This segment is approximately half of an oscillation period in length. The resulting distribution of the correlation coefficient marks each individual half oscillation cycle (figure 4, right). With this information, a phase angle is assigned to each simultaneously recorded PIV snapshot. All data within a prescribed phase angle window are averaged. The size of the phase angle window is 3° for the present study which was identified by Ostermann et al (2015a) as the most suitable for the given data set because it sufficiently reduces noise while maintaining the detailed flow features. It is verified that the averaging process for each window converges. All PIV measurement windows and pressure data are phase-averaged in the described manner. Figure 5 compares an instantaneous PIV snapshot with the respective phase-averaged velocity field for an arbitrary phase angle. The phase-averaged flow field visualizes the same features at a reduced noise. Additional information on the method and its validation can be found in Ostermann et al (2015a).

The autocorrelation method does not provide a consistent starting point for all windows. Therefore, they are phase-aligned based on the phase-averaged pressure signal. The windows' position is chosen so that a sufficient overlap is maintained in order to assess the agreement between different measurements and to provide a smooth transition between the windows. The smooth transition is achieved by a weighted average of the overlapping data points. With this process, the entire internal and external flow field is available for one oscillation cycle with high spatial and temporal resolution. However, the definition of the cycle starting point remains arbitrary. The literature does not offer any quantitative definition. Usually any reference to phase angles is based on qualitative criteria such as the jet's internal or external deflection state. In the current study, the cycle start is chosen to be the zero difference (with a sign change from negative to positive) in the reference signal which refers to the zero differential pressure between the two feedback channel inlets. Qualitatively, this definition marks the instance where the jet exits the oscillator at
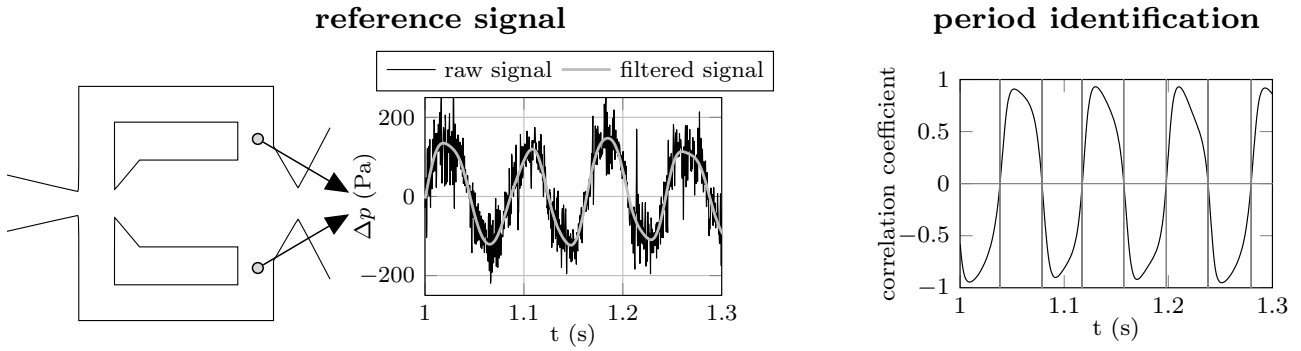
reference signal

period identification

Fig. 4 Period identification from an improved reference signal. Differential pressure signal from two taps (left). Period identification based on correlation method (right).
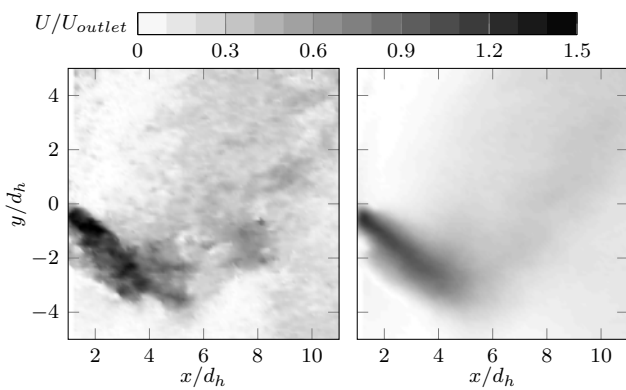

Fig. 5 Comparison between a PIV snapshot (left) and the appropriate phase-averaged flow field (right)

Fig. 6 The jet's oscillation frequency vs. supply rate

almost zero deflection. However, this definition and the accompanying qualitative observations are specific to the particular oscillator used in this study and would be different for other oscillator designs and sizes.

4 Results

The aforementioned phase-averaging method yields the continuous internal and external flow field for various supply rates which range from 0.7 to 27.8 g/s. Figure 6 illustrates the mean oscillation frequency f as a function of outlet velocity U_{outlet}, supply rate $\dot{m}$, and Reynolds number Re. The frequency is obtained from spectral analysis of the pressure data. The outlet velocity is based on the smallest cross-section in the oscillator's outlet nozzle and on the assumption of ambient conditions at the outlet. With a calculated Mach number of 0.11 for the highest mass flowrate, this assumption is well within the common limits of incompressibility. The Reynolds number is based on the outlet velocity and the hydraulic diameter (i.e., $d_h = 25$ mm) of the square outlet. It is noted that all Reynolds number values are within the
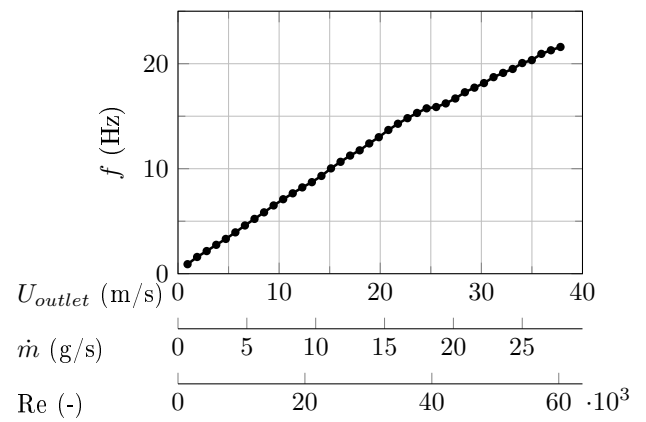
turbulent regime of a common pipe flow. As expected, the oscillation frequency increases linearly with supply rate which has been observed in almost all literature on fluidic oscillators. The linear trend is also evident for very low supply rates ($U_{outlet} \leq 1$ m/s). Therefore, even lower oscillation frequencies than 1 Hz may be achievable. A minimum supply rate required to obtain oscillations is not noticed in this study. A small deviation from the linear dependency of f is observed around $U_{outlet} = 25$ m/s. This deviation is caused by subtle changes in the internal dynamics which have a significant impact on the jet's maximum deflection angle. More detail on these changes is discussed in the subsequent section.

The time-resolved information of the flow field is examined to address the internal dynamics such as the switching mechanism, and the oscillation pattern of the external jet. For structural clarity, the internal and external flow field are addressed individually in the following two sections. All flow field discussions are based on $U_{outlet} = 15$ m/s (Re = 25,000, Ma = 0.04) because this value yields representative results. In addition, selected properties are examined as a function of supply

rate. Note that all supply rates are well within the incompressible regime.

4.1 Internal Dynamics

The internal flow field is characterized by various dynamics especially within the mixing chamber and feedback channels. Figure 7 (left) visualizes the internal distribution of the velocity magnitude U for various phase angles ϕ during half an oscillation cycle. The right column of figure 7 illustrates the respective streamlines to enhance the visibility of the dynamics. The number, integration length, and origin of the streamlines is kept constant for all phase-angles. The streamlines should solely be regarded as a tool for visualization because they not provide a quantitative measure of vortex strength or velocity magnitude. An animation of the internal flow field including the streamlines and velocity magnitude is available in a supplemental video (Online Resource 1). Additionally, an animation of the time-resolved Finite-Time-Lyapunov-Exponent (FTLE) based on Haller (2001) is available in Online Resource 2. This exponent reveals detailed flow dynamics inside the oscillator. Both videos are intended to complement the following discussion.

At the start of the cycle ($\phi = 0°$), the main jet is in the process of attaching to the upper wall of the mixing chamber. The jet separates at the sharp inlet wedge and encloses a separation bubble with the wall. It should be noted that without any feedback channels the jet would remain attached in a stable state and the jet would steadily exit the device at a fixed deflection. Instead, the jet impinges on the converging wall of the outlet nozzle which directs a portion of the fluid into the upper feedback channel ($\phi = 60°$). This fluid returns to the inlet where it feeds into the separation bubble at a low momentum. The bubble grows in size and moves downstream, thereby pushing the main jet off the wall ($\phi = 120°$). The resulting curvature of the main jet increases the impingement angle on the outlet nozzle wall which in turn diverts even more fluid into the feedback channel. This self-amplifying process causes a rapid growth of the separation bubble which eventually pushes the main jet entirely to the opposite side ($\phi = 180°$). There, it encloses a new separation bubble with the lower wall which initiates the switching mechanism with the opposite side. The separation bubble from the upper wall opens into the feedback channel inlet and dissipates with the decreasing flow through the feedback channel. This dissipation can be tracked with the remnants of the separation bubble from the lower wall.

The process of fluid feeding into the separation bubble is identified as the underlying mechanism for the switching of the jet. If the shape of the mixing chamber walls is more streamlined so that no initial separation bubble is present, the fluid from the feedback channels just pushes in between the main jet and the wall to deflect it to the opposite side (Ostermann et al 2015b). Besides the described switching mechanism, a few additional dynamics are noteworthy. At the start of the cycle ($\phi = 0°$), it is evident that parts of the main jet are shaved off by the inlet wedge to penetrate into the feedback channel outlet. In combination with the opposing flow from the channel inlet, a pair of vortices forms in the left corner. These vortices persist until they are overcome by the flow entering the feedback channel inlet. The described dynamic is likely to delay the jet attachment process and the initiation of a sustained stream into the feedback channel inlet. A larger distance between the wedges may reduce this effect and thereby accelerate the switching process which in turn would yield an increased oscillation frequency for the same supply rate. This suggestion was verified numerically by Bobusch et al (2013b). Additional detail on the mass flow through the feedback channels is discussed shortly.

Another observation relates to flow separation within the feedback channels. At various instances throughout an oscillation cycle, the flow separates around the sharp inside corners of the channel path and forms recirculation areas in the outer corners. This separation causes unnecessary losses and a reduction of the effective channel width. A more streamlined channel geometry can potentially increase the oscillator's performance. An essential part of the oscillator's geometry is the shape of the outlet nozzle. The angle and shape of the converging nozzle walls are expected to determine the amount of fluid being diverted into the feedback channel which affects the switching process and therefore the oscillation frequency. Furthermore, the angle also governs the jet's deflection at the outlet which may be altered by adjusting the divergence angle or shape. It should be noted that the emitted jet does not, at any instance, attach to the diverging nozzle walls. Therefore, this part of the nozzle may be omitted which may be beneficial for some applications. However, a smaller divergence angle may force the jet to attach to this wall and thereby increase the jet's maximum deflection (Ostermann et al 2015b). Some initial alterations of the nozzle geometry were also investigated by Bobusch et al (2013b).

As previously mentioned, the flowrate through the feedback channels is a governing parameter for the internal oscillation mechanism. It was suggested experimentally and numerically by Bobusch et al (2013a,b) that the total volume of fluid transported through the feedback channel during one oscillation cycle is independent of the supply rate at least within the incompressible regime. This observation is explained with the separation
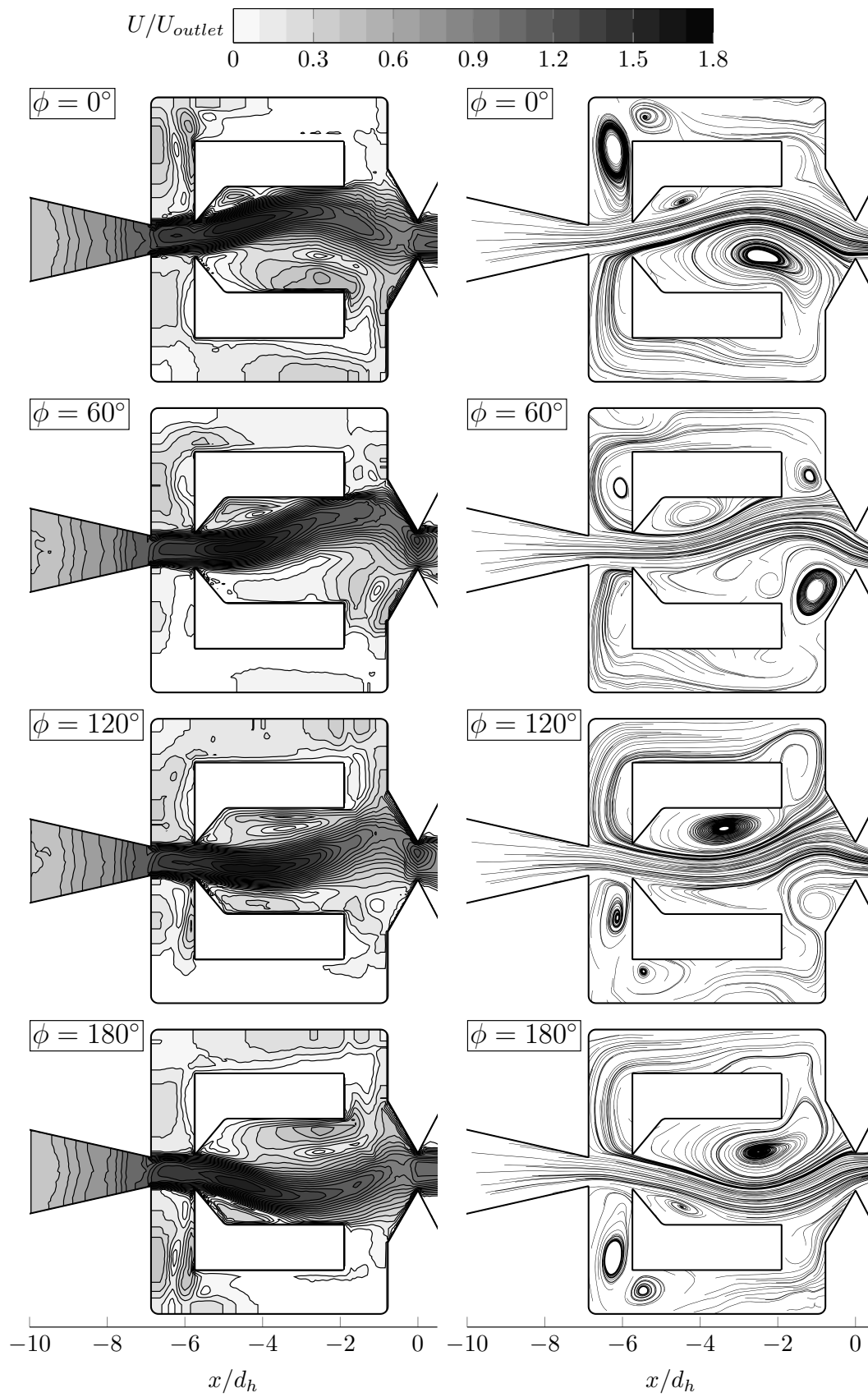
Fig. 7 The oscillator's internal flow field (left) and corresponding streamlines (right)
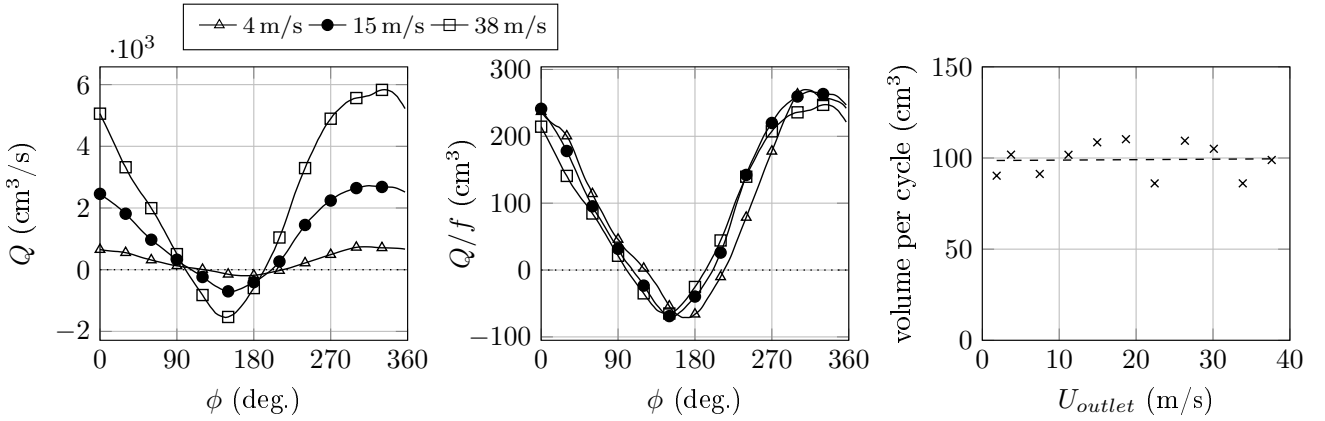
Fig. 8 Volume flow through lower feedback channel (every 10th data point marked)(left). The same volume flow normalized by the corresponding oscillation frequency (every 10th data point marked)(center). Total volume transported through feedback channel per oscillation cycle (right).

bubble between the main jet and wall having to grow by a fixed but design-specific volume to push the jet to the opposite side. This hypothesis is confirmed in the current study for air as the working fluid. Figure 8 (left) shows the volume flow Q through a cross-section at the center of the feedback channel for various supply rates. As expected, the extreme values increase with supply rate due to the increasing internal velocities. However, the volume flowrates occur over shorter periods of time because of the shorter cycle durations. When normalized by the oscillation frequency (figure 8, middle), the data collapse onto a single curve within the measurement accuracy. This infers that the total volume transported through the feedback channel per oscillation cycle is independent of supply rate. The argument is confirmed in figure 8 (right) by integrating the flowrate over one cycle for the entire range of considered supply rates. The data scatter is likely due to the limited spatial resolution over the small width of the feedback channel. However, a linear regression indicates the constant total volume. This result supports the argument that the volumetric growth of the recirculation bubble is the underlying mechanism governing the switching process. Further evidence for this statement is visualized in figure 9. The growth of the recirculation bubble from its initial size to its maximum extent is outlined. The difference in area multiplied by the oscillator depth matches the total volume per oscillation cycle (figure 8, right). These findings infer that the oscillation frequency mainly depends on the time it takes to transport the required volume through the feedback channel. This implies that the oscillation frequency may be increased by improving the flowrate through the feedback channel or by reducing the required total volume.

Although the internal dynamics appear to be very consistent and widely independent of supply rate, some
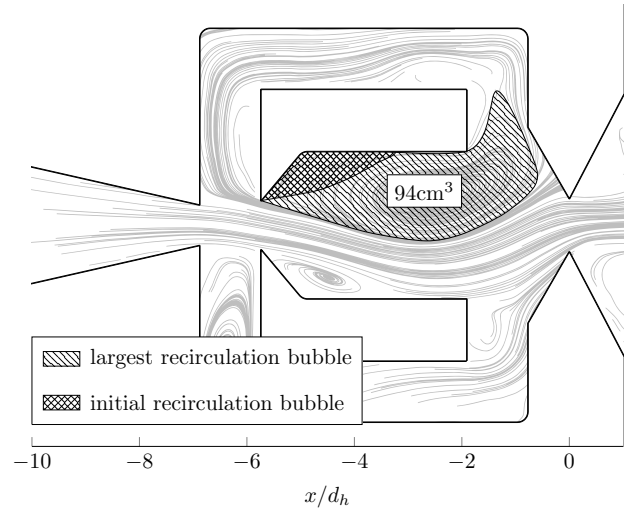

Fig. 9 Estimation of volume fed to the recirculation bubble.
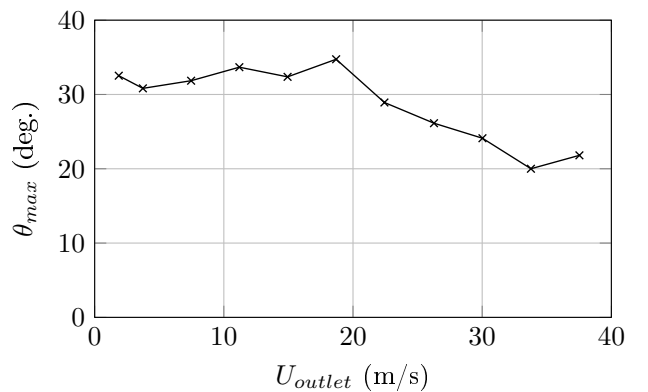

Fig. 10 Maximum jet deflection angle at the outlet

changes take place at higher velocities. These changes are not just noticed in the frequency shift at around $U_{outlet} = 25\,\mathrm{m/s}$ (figure 6) but are most obvious in the jet's maximum deflection at the outlet. The deflection
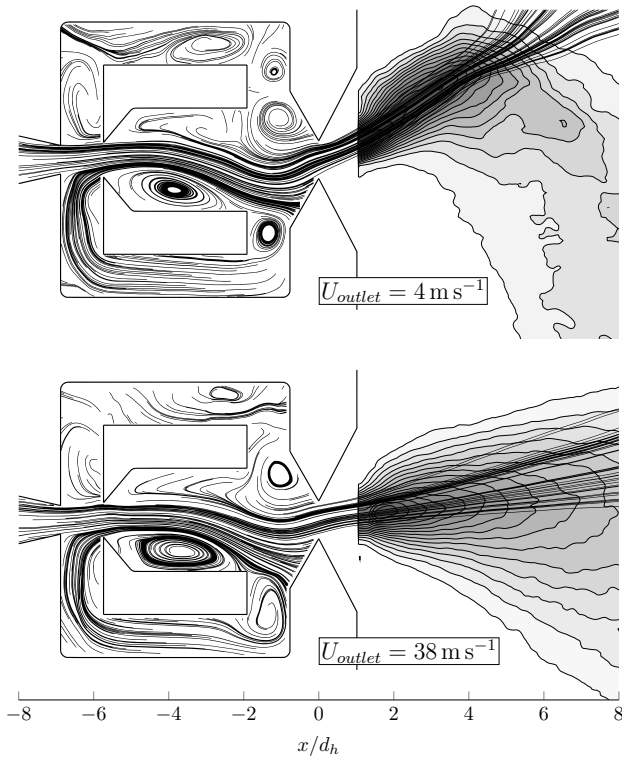
Fig. 11 Instantaneous internal and external flow field for two supply rates ($\phi = 267°$)

Fig. 12 Time-averaged pressure difference in the feedback channel

angle θ is obtained from the u and v component of the highest velocity magnitudes. Figure 10 depicts this angle at the outlet as a function of the supply rate. A significant drop in θ_{max} is observed at a similar value for U_{outlet} where the discrepancy in frequency occurs. These differences are visualized by the internal and external flow field for a small and a large supply rate at the same phase angle (figure 11). It is apparent that the jets' external deflection angles differ significantly. However, the internal changes are not as obvious. The main difference between the two supply rates is observed in the area of the feedback channel inlet. For the higher supply rate, the cavity vortex formed at the inlet is larger and extends deeper into the feedback channel. This affects the jet's approach path to the inner wall of the outlet nozzle which has a significant impact on the jet's exit angle. It is not exactly clear what causes the changing vortex dynamics at the feedback channel inlet. The main reason is suspected to be the internal jet width which increases with supply rate due to increasing turbulence levels. As noted in figure 8 (left), the increased jet width amplifies the reversed flow into the feedback channel outlet which also impacts the dynamics at the feedback channel inlet. Furthermore, the larger jet width within the mixing chamber affects the dynamics due to the confined space of the internal geometry. As previously
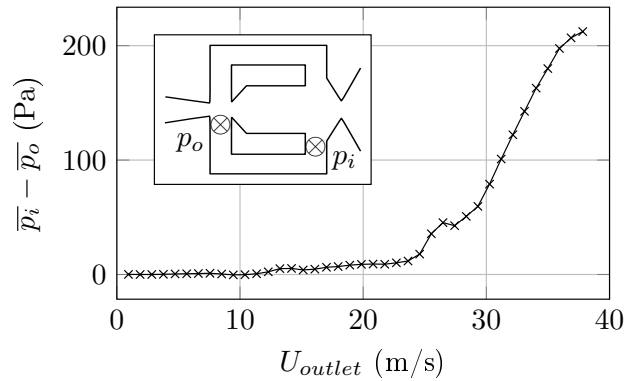
suggested, the shape and geometry of the nozzle's inner walls are a determining factor for the jet's external deflection. Although the changes in jet width are gradual, a threshold value may be reached beyond which the jet's impingement onto the wall is altered with significant consequences. Because it is suggested that the changing dynamics are most evident within the feedback channel, the pressure difference between its inlet and outlet ought to be most revealing. Figure 12 presents the time-averaged pressure difference between the inlet and outlet as a function of supply rate. An almost unchanged behavior is noticeable up to $U_{outlet} \approx 25 \, \text{m/s}$ before a rapid increase in pressure difference occurs, which is consistent with the discrepancy in oscillation frequency and the decline in deflection angle.

4.2 External Dynamics

The previous discussion of the internal dynamics relates directly to the external flow field properties which are of particular interest in view of potential applications. In this section, a general overview of the external flow field is provided, followed by an evaluation of the oscillation pattern based on the instantaneous deflection angle. Furthermore, the properties of the jet at the outlet are discussed. Two corresponding animations are available in Online Resource 3 and 4. The video in Online Resource 3 depicts the external FTLE field similar to the corresponding video for the internal flow field (Online Resource 2). The video in Online Resource 4 combines the internal and external flow field with the velocity magnitude. Again, these animations are intended to complement the following discussions.

Figure 13 illustrates the instantaneous velocity magnitude throughout the external flow field for half an oscillation cycle. For comparison, the flow field of a steady jet is added. This jet originates from the same device with sealed feedback channels and streamlined
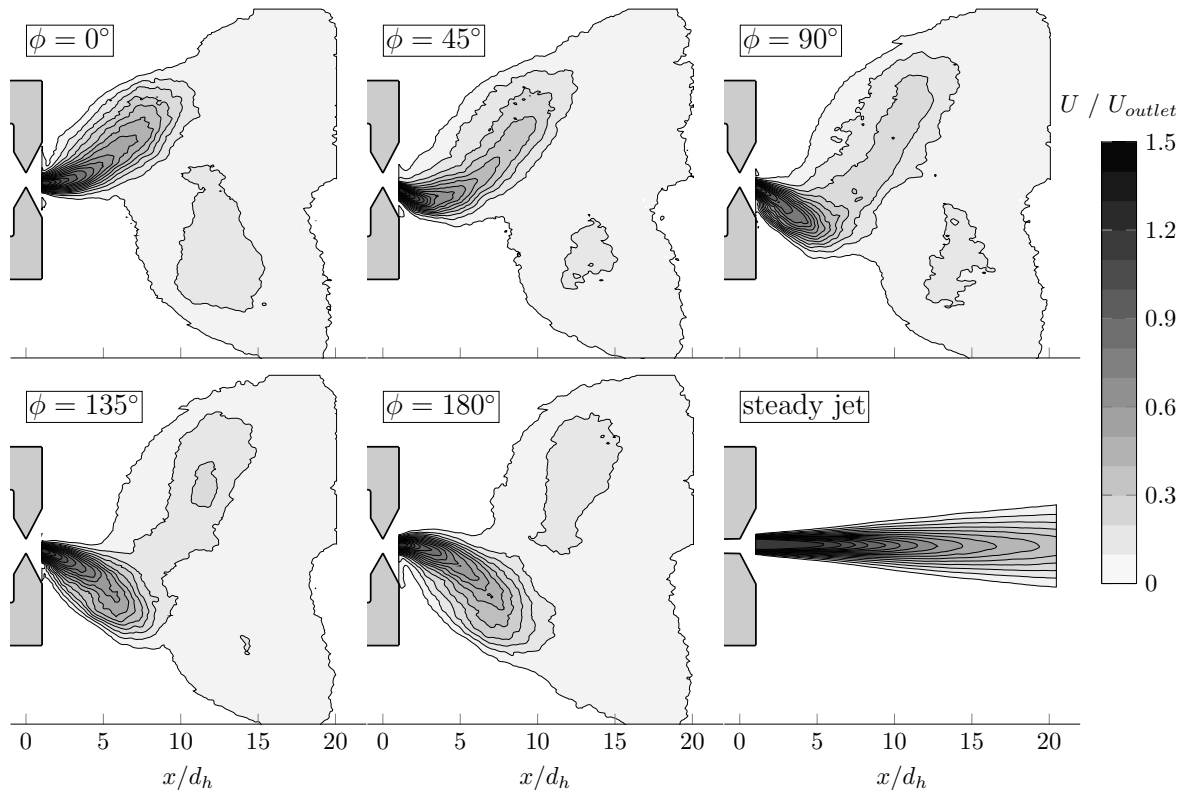
Fig. 13 Half oscillation period of the external flow field

mixing chamber. Note that the coordinate origin is located in the center of the smallest nozzle cross-section. Due to the sweeping motion of the jet, the impacted area is substantially larger than that of the non-oscillating jet. The lateral extent of the affected region is almost twice as large as the corresponding distance from the nozzle, which is consistent with the maximum deflection angle being close to $\pm 45°$. This large impact zone is the key feature of fluidic oscillators, especially for applications where a widespread distribution of fluid is desired. One distinct observation is made at the outer edge of the jet when fully deflected (figure 14, left). A vortex forms due to the shear layer. However, only one vortex develops, moves downstream, and dissipates when the jet switches back to the opposite side. This observation may explain the seemingly stationary pair of vortices detected in other studies (e.g. Woszidlo et al 2014) with a surface pattern visualization on an adjacent wall (figure 14, right). The time-averaging effect of the visualization technique depicts an enlarged footprint of the vortex on both sides of the jet's sweeping range although the presence of the vortices alternates. Even though the jet's sweeping motion only enables the formation of distinct vortices at the outer edges, the steep velocity gradients cause a significant distribution of vorticity over the entire affected area.
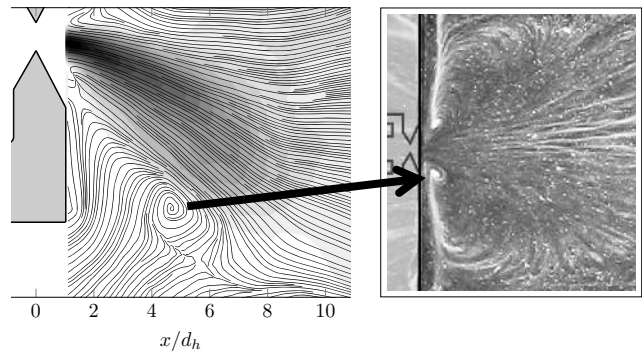

Fig. 14 Vortex in the external flow field in comparison to a flow visualization (Woszidlo et al 2014)

In view of applications which require a particular oscillation pattern, the time-resolved deflection angle is of interest. The oscillation pattern is assessed by obtaining the jet deflection from each instantaneous jet profile throughout one oscillation cycle (figure 15). Because of the jet's considerable lateral extent, an appropriate comparison of the jet's properties at different instances in time has to be performed at a fixed radial distance from the nozzle. Therefore, the coordinate system is transformed to polar coordinates with the polar angle ψ and radial distance r. In figure 15, the jet's instantaneous deflection angle is obtained along an arch with $r/d_h = 1.4$.

The first impression indicates a smooth and approximately sinusoidal oscillation pattern (figure 15, top). However, a more detailed analysis of the jet's transient behavior reveals a distinct overshoot in the deflection angle and changing oscillation speeds. Therefore, the angular velocity of the changes in deflection is calculated (figure 15, bottom), which reveals more distinct features. Three phases are defined within the pattern. The first phase corresponds to the mentioned overshoot in jet deflection, which is characterized by a rapid decrease in angular velocity up to the maximum deflection angle. The jet does not reside at this angle and quickly moves back to a smaller deflection where it remains with a decreasing angular velocity. This behavior is referred to as the "deceleration" phase. It is followed by a fast acceleration which marks the movement of the jet to the opposite side (i.e. acceleration phase). Based on these phases, two characteristic time scales are defined. During the overshoot and deceleration phase the jet is considered to be in its deflected state. The associated duration is referred to as the "dwelling time". The duration of the acceleration phase is named the "switching time". These two time scales are assessed for the entire range of considered supply rates (figure 16). Based on these definitions, the jet dwells on the sides for approximately as long as it takes to switch to the opposite side. Although the maximum deflection decreases significantly (figure 10), the same external oscillation pattern is observed. Therefore, the respective time scales remain almost unchanged. In relation to the internal flow field, one more interesting observation can be made from the transient jet deflection. The maximum jet deflection angle is obtained at approximately $\phi = 60°$, which does not coincide with the internal jet being fully attached to one of the walls as may be expected. Instead, the maximum deflection occurs while the internal jet is switching from one side to the other.

Although the sweeping pattern appears smooth and sinusoidal, the instantaneous jet properties at different deflections vary significantly. Figure 17 identifies these variations at the outlet. The jet properties oscillate by up to 10% around their corresponding mean value. Note that the mass flow and momentum are based on the depth of the outlet. The phase angles for the extreme values in jet velocity, mass flow, and momentum coincide. Furthermore, the minima in jet width (i.e. the normal width of the local velocity profile with $U \geq 50\% \, U_{max}$) correspond to the maxima in jet deflection angle. Because the jet exits the nozzle at an off-center angle, the effective outlet size is reduced. The opposite is true for the zero deflection angle, which is accompanied by the largest jet width and the smallest jet velocity. The oscillation in mass flow can be explained by two observa-
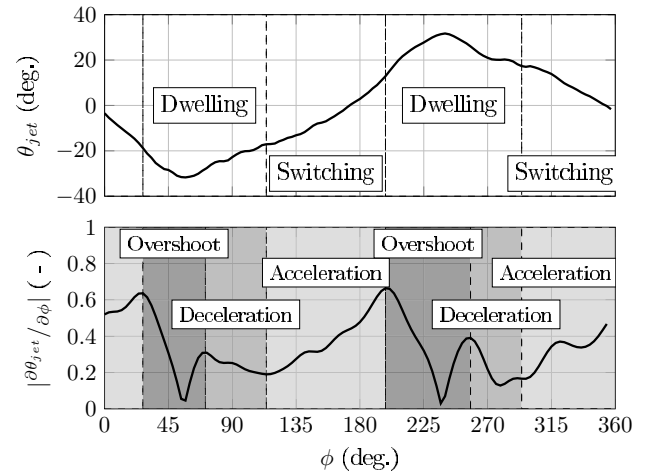

Fig. 15 Time-resolved deflection angle (top) and corresponding angular velocity (bottom) at $r/d_h = 1.4$
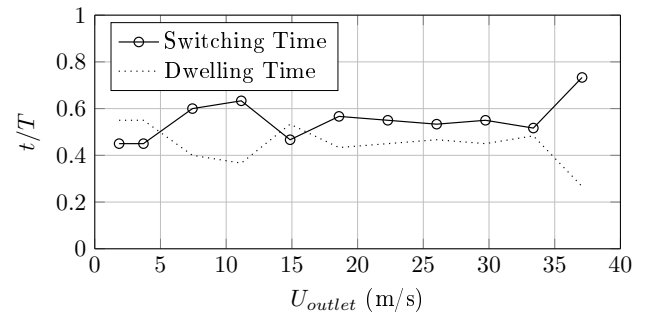

Fig. 16 Oscillation time scales as a function of the supply rate ($r/d_h = 1.4$)

tions. The first observation is the blockage effect of the growing recirculation bubble. Due to its size, the bubble presents considerable blockage to the mass flow supply. The second observation is the impingement of the jet on the converging walls of the outlet nozzle which causes a significant adverse pressure gradient. The oscillations in pressure are even detected in the settling chamber upstream of the oscillator. At the largest extent of the separation bubble at approximately $\phi = 180°$ (figure 7), the blockage effect is at its maximum and the jet impinges on the inner nozzle wall. This instance coincides with the minimum in mass flow at the outlet (figure 17). Therefore, these effects work in tandem for this particular oscillator geometry. However, the relative impact of either effect can not be quantified with the existing data set and oscillator geometry. Similar oscillations in the jet's properties were observed by Bobusch et al (2013a) with water as a working fluid. These findings may affect the oscillator's applications, especially if an even distribution of fluid is desired. No information is available yet to whether the oscillatory output impacts the performance for flow control purposes.
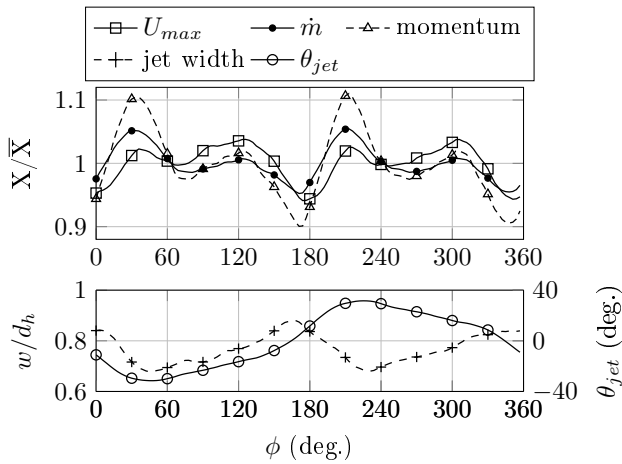
Fig. 17 Jet properties at the outlet. Every 10th data point marked

The instantaneous properties of the jet (e.g., jet velocity and jet width) may also be evaluated in the external flow field. Gaertlein et al (2014) suggested that the jet width is increasing with radial distance at a higher rate than a corresponding steady jet. At the same time, the jet's velocity is decaying faster with radial distance. However, these observations are solely based on two-dimensional flow field data which neglects a potential meandering of the jet in and out of the laser plane. Gaertlein et al (2014) also estimate the entrainment of the jet by introducing an effective jet depth based on the conservation of momentum. Although this estimation suggests that the oscillating jet entrains substantially more fluid than a steady jet, its accurate quantitative determination requires three-dimensional flow field information. Therefore, the quantitative evaluation of the external flow field is left for future studies.

5 Conclusion

The presented work examines the time-resolved internal and external flow field of a fluidic oscillator within the incompressible regime. Time-resolved pressure and PIV data are phase-averaged based on a simultaneously recorded reference signal in the feedback channel inlets. The underlying mechanism governing the jet's oscillatory movement is identified from the internal flow field. A recirculation bubble between the jet and the chamber wall grows by fluid from the feedback channels feeding into it. The growing bubble pushes the jet off the wall and over to the opposite side. Although the flowrate through the feedback channel increases with jet velocity, the total transported volume per oscillation cycle remains independent of supply rate. This volume is confirmed to match the volumetric growth of the recirculation bubble.

Therefore, the oscillation frequency is mainly dependent on the required volumetric growth and on how fast this required volume is provided through the feedback channels. The study of the internal dynamics leads to various potential design modifications. The initial separation bubble may be averted entirely by streamlining the inner walls of the mixing chamber. Furthermore, the feedback channels may be streamlined to prevent unnecessary losses due to separation. The amount of fluid diverted into the feedback channels and the jet's deflection angle are most influenced by the design of the outlet nozzle.

Although the internal dynamics are consistent over the range of considered supply rates, some subtle changes occur. These changes are attributed to an increased jet width due to increasing turbulence levels. A wider jet causes increased reversed flow through the feedback channels, which affects the jet's impingement angle on the inner nozzle walls. Once a certain threshold value is reached, the jet's maximum deflection angle drops significantly. Despite the changes in deflection angle, the oscillation pattern is consistently sinusoidal. The jet spends a comparable amount of time for dwelling in its deflected state and for switching over to the opposite side. During the oscillatory movement, the jet's properties also oscillate by up to 10% around their mean value at the exit. The sweeping pattern in conjunction with the oscillatory output are significant features when considering the oscillators' applications. Especially when a homogenous distribution of fluid is desired, these characteristics have to be designed accordingly. Their relevance to flow control applications is currently unknown but should be addressed in future research.

In summary, it should be noted that the described observations of the internal and external dynamics may be specific to the investigated oscillator geometry and therefore may be different for other designs. However, the results provide some fundamental insight and potential guidelines for the development and optimization of fluidic oscillators with specific properties.

References

Bobusch BC, Woszidlo R, Bergada JM, Nayeri CNN, Paschereit CO (2013a) Experimental study of the internal flow structures inside a fluidic oscillator. Experiments in Fluids 54(6), doi:10.1007/s00348-013-1559-6

Bobusch BC, Woszidlo R, Krüger O, Paschereit CO (2013b) Numerical investigations on geometric parameters affecting the oscillation properties of a fluidic oscillator. AIAA 21st Computational Fluid Dynamics Conference doi:10.2514/6.2013-2709

Cerretelli C, Kirtley K (2009) Boundary layer separation control with fluidic oscillators. Journal of Turbomachinery 131(4), doi:10.1115/1.3066242

Gaertlein S, Woszidlo R, Ostermann F, Nayeri CN, Paschereit
CO (2014) The time-resolved internal and external flow field
properties of a fluidic oscillator. 52nd Aerospace Sciences
Meeting doi:10.2514/6.2014-1143

Gregory J, Tomac MN (2013) A review of fluidic oscilla-
tor development. AIAA 43rd Fluid Dynamics Conference
doi:10.2514/6.2013-2474

Gregory JW, Sullivan JP, Raman G, Raghu S (2007) Char-
acterization of the microfluidic oscillator. AIAA Journal
45(3):568–576, doi:10.2514/1.26127

Gregory JW, Gnanamanickam EP, Sullivan JP, Raghu S
(2009) Variable-frequency fluidic oscillator driven by a
piezoelectric bender. AIAA Journal 47(11):2717–2725,
doi:10.2514/1.44078

Guyot D, Paschereit CO, Raghu S (2009) Active combustion
control using a fluidic oscillator for asymmetric fuel flow
modulation. International Journal of Flow Control 1(2):155–
166, doi:10.1260/175682509788913335

Haller G (2001) Lagrangian structures and the rate of strain in
a partition of two-dimensional turbulence. Physics of Fluids
13(11):3365, doi:10.1063/1.1403336

Luxton RE, Nathan G (1991) Controlling the motion of a fluid
jet. Patent, US 5060867 A

Ostermann F, Woszidlo R, Gaertlein S, Nayeri CN, Paschereit
CO (2015a) Phase-averaging methods for the natural flow
field of a fluidic oscillator. AIAA Journal (accepted for
publication)

Ostermann F, Woszidlo R, Nayeri CN, Paschereit CO (2015b)
Experimental comparison between the flow field of two
common fluidic oscillator designs. 53rd AIAA Aerospace
Sciences Meeting

Phillips E, Wygnanski I (2013) Use of sweeping jets during
transient deployment of a control surface. AIAA Journal
51(4):819–828, doi:10.2514/1.j051683

Raghu S (2001) Feedback-free fluidic oscillator and method.
Patent, US 6,253,782 B1

Raman G, Raghu S (2004) Cavity resonance suppression us-
ing miniature fluidic oscillators. AIAA Journal 42(12):2608–
2612, doi:10.2514/1.521

Seele R, Tewes P, Woszidlo R, McVeigh MA, Lucas NJ, Wygnan-
ski IJ (2009) Discrete sweeping jets as tools for improving
the performance of the V-22. AIAA Journal of Aircraft
46(6):2098–2106, doi:10.2514/1.43663

Spyropoulos CE (1964) A sonic oscillator. Harry Diamond Lab-
oratories pp 27–52

Stouffer R (1979) Oscillating spray device. Patent US 4151955

Wassermann F, Hecker D, Jung B, Markl M, Seifert A, Grund-
mann S (2013) Phase-locked 3D3C-MRV measurements in
a bi-stable fluidic oscillator. Experiments in Fluids 54(3),
doi:10.1007/s00348-013-1487-5

Woszidlo R, Wygnanski IJ (2011) Parameters governing separa-
tion control with sweeping jet actuators. AIAA 29th Applied
Aerodynamics Conference doi:10.2514/6.2011-3172

Woszidlo R, Stumper T, Nayeri CN, Paschereit CO (2014) Exper-
imental study on bluff body drag reduction with fluidic oscil-
lators. 52nd Aerospace Sciences Meeting doi:10.2514/6.2014-
0403